

A general tensor prediction framework based on graph neural networks

Hongjun Xiang (✉ hxiang@fudan.edu.cn)

Fudan University <https://orcid.org/0000-0002-9396-3214>

Yang Zhong

Fudan University

Hongyu Yu

Fudan University

Xinggao Gong

Fudan University

Article

Keywords:

Posted Date: August 3rd, 2022

DOI: <https://doi.org/10.21203/rs.3.rs-1900756/v1>

License: © ⓘ This work is licensed under a Creative Commons Attribution 4.0 International License.

[Read Full License](#)

Abstract

Graph neural networks (GNNs) have shown extremely high flexibility and accuracy in predicting the physical properties of molecules and crystals. However, traditional invariant GNNs are not compatible with directional properties, which currently limits their application only to the prediction of invariant scalar properties. To address this issue, here we propose a general framework, i.e., an edge-based tensor prediction graph neural network (ETGNN), where a tensor is expressed as the linear combination of the local spatial components projected on the edge directions of multiple-sized clusters. This tensor decomposition is rotationally equivariant and exactly satisfies the symmetry of the local structures, while the coefficients before each local spatial component are rotationally invariant scalars which can be easily predicted by traditional invariant GNNs. The accuracy and universality of our new framework are demonstrated by the successful prediction of various tensor properties from first-order to third-order. The framework proposed in this work will enable GNNs to step into the broad field of the prediction of directional properties.

Introduction

The development of machine learning (ML) is changing the traditional research paradigm of molecular and material science¹⁻³. Without performing the computationally demanding electronic structure calculations, ML can build an end-to-end mapping from structure to properties based on the large databases to accelerate materials development⁴⁻¹². In addition, machine learning atomic potential with quantum-mechanical precision has been widely used to replace the costly first-principles calculations¹³⁻¹⁶. The successful applications of ML in computational material science are largely because the adopted framework conforms with the fundamental symmetries of the system. As in the case of the traditional graph neural networks (GNNs)¹⁷⁻²² and classical kernel-based machine learning methods²³⁻²⁶, the translational and rotational invariant features of the scalar properties are exploited to increase the accuracy and transferability for the prediction of scalar properties.

Besides invariant scalar properties, various tensorial properties of materials are also important to material functions. The tensorial properties of materials describe the response susceptibilities of materials to various external fields. For example, the dielectric tensor describes the response of an insulator to the electric field. The piezoelectric tensors describe the anisotropic response of materials to mechanical perturbations. The prediction of tensorial properties requires the models to be rotationally equivariant when the reference coordinate system is rotated. Most of the recently proposed equivariant networks are based on $SO(3)$ representations to incorporate directional information²⁷⁻³⁰. Since these conceptually complex networks use inconvenient Clebsch-Gordan (CG) transforms on spherical harmonic bases to achieve equivariance, the conversion between one-dimensional $SO(3)$ equivariant features and higher-order geometric tensors is not straightforward. So far, these networks have been reported to achieve very high accuracy in scalar prediction tasks but have rarely been used to predict the tensor properties of molecules and crystals³¹⁻³³.

In molecular and material science, Gaussian Process Regression (GPR) based on an equivariant kernel is the earliest network architecture for tensor prediction. Grisafi *et al.* proposed a GPR equivariant model based on the symmetry-adapted Smooth Overlap of Atomic Positions (SOAP) kernels to predict the tensorial properties³⁴. In this GPR framework, the geometric tensors are decomposed into a series of irreducible spherical tensor (IST) representations which can be learned independently. Recently, Nguyen *et al.* have further represented each IST component as a sum of each atomic tensor that is represented by a local atomic environment descriptor defined by a linear combination of spherical harmonics³⁵. These kernel methods based on IST decomposition rely on the construction of the fixed equivariant kernels to predict tensors. Hence its accuracy and multi-element generalization ability may be limited. Since the more flexible GNNs can learn a representation in a self-adaptive way and a single GNN can simultaneously deal with all elements in the whole periodic table, it is expected that GNNs would predict tensors more accurately than the usual descriptor-based ML approaches, similar to the case of predicting scalar properties. Unfortunately, the usual invariant GNNs can not be straightforwardly adopted to predict the equivariant tensor properties. Some modified GNNs for tensor prediction have been reported recently. Glick *et al.* proposed a Cartesian message passing neural network (CMPNN) by introducing directional edge features between adjacent atoms to encode the Cartesian information³⁶. This model successfully predicted atomic multipole moments. However, the message functions and update functions of this architecture have the same form as their invariant counterparts. Although this model adopted the data augmentation technique, the equivariance of tensors is not strictly satisfied. Clearly, a general GNN-based framework for accurately predicting tensors is highly desirable.

In this Letter, we proposed a tensor prediction framework based on GNNs. The main idea of this framework is that the tensor property of a crystal can be represented as the average of the tensor contributions of all the atoms in the crystal and that the tensor contribution of each atom can be expressed as the linear combination of the local spatial components projected on the edge directions of multiple-sized clusters. This framework can describe the general tensors of different orders and symmetries. To implement this framework, we designed an *edge-based tensor prediction graph neural network* (ETGNN) and tested its tensor prediction ability for a wide range of tensors including the forces (\vec{F}), dipole moments (μ), polarizabilities (a), chemical shifts (σ), Born effective charges (BECs), dielectric (DL), and piezoelectric (PZ) tensors. This approach is conceptually simple and enables various GNNs to be able to predict tensors without making significant changes to the existing networks.

Results And Discussion

Theory

The equivariance of a tensor refers to the behavior that the tensor changes under the transformation of the coordination system, in contrast to the invariance of the scalar (e.g., the energy) which remains unchanged. The traditional GNNs embed the scalar information of graphs such as species and inter-atomic distance into the invariant features of nodes and edges, which are updated iteratively. GNNs in

molecular and materials science widely adopt the atom-centric scalar prediction framework³⁷, which expresses the energy of a crystal as the sum of the atomic energies predicted by the invariant features of atoms. Here, we generalize the atom-centric framework of GNNs to tensors and represent each crystal rank- M tensor property (T^M) as the average of the atomic rank- M tensor contributions (T_j^M). The key to the problem is how to predict the atomic tensors. The illustration of predicting the atomic rank- M tensors in this framework is shown in Fig. 1. This tensor prediction framework can be expressed by the following formulas:

$$T^M = \frac{1}{N} \sum_{j=1}^N T_j^M,$$

1

$$T_j^M = \sum_{k_i \in N(j)} t_{k_1 k_2 \dots k_n j} (\vec{e}_{k_1 j})^{\otimes f_1} \otimes (\vec{e}_{k_2 j})^{\otimes f_2} \otimes \dots \otimes (\vec{e}_{k_n j})^{\otimes f_n},$$

2

where N is the number of atoms in the cell, and $\vec{e}_{k_i j}$ is the unit edge vector from the neighboring atom k_i to the central atom j . $N(j)$ represents the set of all neighbor atoms of atom j within a cutoff radius r_c . $(\vec{e}_{k_i j})^{\otimes f_i}$ is the f_i -fold ($f_i \geq 1$) tensor product of $\vec{e}_{k_i j}$, and $\sum_{i=1}^n f_i = M$. $t_{k_1 k_2 \dots k_n j}$ is a scalar coefficient of the cluster containing n individual neighboring atoms, which can be derived from the features $m_{k_1 k_2 \dots k_n j}$ of the j -centered cluster. The summation in Eq. (2) runs over all the permutations of n neighbors of atom j . Eq. (2) is a general expression of the atomic rank- M tensor expansion which requires at most M individual edge vectors to construct the tensor bases. For symmetric crystal tensors, we can represent it as the average of the symmetric atomic tensors which can be expanded with the symmetric tensor bases. In this case, n can be smaller than M since the symmetric tensor bases can be constructed by the multi-fold tensor product of the edge vectors. This can greatly reduce the complexity of the formulas and the amount of unnecessary calculations.

One can easily show that the tensors predicted by ETGNN strictly satisfy the equivariance condition. The tensor product of two vectors $u^{(l_1)}$ and $v^{(l_2)}$ of orders l_1 and l_2 is a prescription to obtain another equivariant vector or tensor $(u \otimes v)^{(l_1 \otimes l_2)}$ in a higher-order vector space. Since each edge vector in the real space is rotationally equivariant, the tensors obtained by the tensor product of multiple edge vectors are also equivariant. Besides, the atomic tensor constructed by Eq. (2) satisfies the proper symmetry of the local structure as all the neighboring atoms [$k_i \in N(j)$] of a central atom (i.e., the j -th atom here) are considered in the summation. If the cluster centered on atom j is symmetric with respect to the rotation or inversion operation R around atom j (i.e., $\forall k_i \in N(j), R \vec{r}_{k_i} = \vec{r}_{k'_i}$, where $k'_i \in N(j)$), then the summation in Eq. (2) remains unchanged. It is a huge advantage that the atomic tensor expansion satisfies the symmetry of the atomic local structures inherently without learning the symmetry of the

local structure through data augmentation or redundant network parameters. We also checked that the tensors predicted by our ETGNN model are indeed compatible with the symmetry of the examined system (see Supplementary Discussion 1 for details). Note that the equivariant tensors constructed by Eqs. (1) and (2) apply to all periodic and nonperiodic systems.

Below we will describe the details of the expansion of the tensors with respect to the edge directions taking force vector, BEC, DL, and PZ tensor as examples. The force vector and BEC of each atom can be directly represented by the corresponding atomic tensor contribution T_j^M , while the dipole moment, DL, and PZ tensors describing the whole crystal are represented by the average of the tensor contributions T_j^M of each atom in the primitive cell.

The force on the j th atom is the sum of the forces from the surrounding neighbor atoms:

$$\vec{F}_j = \sum_{k \in N(j)} t_{kj} \vec{e}_{kj}.$$

3

The coefficients t_{kj} are the magnitude of the forces between the atoms.

Since BEC is an asymmetric second-order tensor, the terms in Eq. (2) are explicitly split into the symmetric part T_j^{sym} and the non-symmetric part $T_j^{non-sym}$:

$$T_j = T_j^{sym} + T_j^{non-sym},$$

4

$$T_j^{sym} = \sum_{k \in N(j)} t_{kj} \vec{e}_{kj} \otimes \vec{e}_{kj},$$

5

$$T_j^{non-sym} = \sum_{\substack{k, i \in N(j) \\ k \neq i}} t_{kji} \vec{e}_{kj} \otimes \vec{e}_{ji}.$$

6

T_j^{sym} is expanded with the second-order symmetric tensor bases $\vec{e}_{kj} \otimes \vec{e}_{kj}$ constructed by the unit direction vectors \vec{e}_{kj} between the atom pairs kj . $T_j^{non-sym}$ is expanded with the asymmetric tensor bases $\vec{e}_{kj} \otimes \vec{e}_{ji}$ constructed by the unit direction vectors \vec{e}_{kj} and \vec{e}_{ji} . Since T_j^{sym} and $T_j^{non-sym}$ require one and two individual neighbor atoms respectively, the expansion coefficients t_{kj} and t_{kji} are mapped from the hidden features of the edge messages (m_{kj}) and the triplet messages (m_{kji}) respectively. The embedding and updating of the triplet messages (m_{kji}) will be illustrated in detail in the

following network implementation section. It is important to note that the expansion formula of BEC can be applied to all second-order atomic tensors.

The DL tensor is a second-order symmetric tensor of the whole crystal and is not extended with the expansion of the primitive cell of the crystal. The DL tensors can be represented as the average of the atomic contributions of the second-order symmetric tensors T_j^{sym} . Therefore, the edge-based expansion of the DL tensor can be written as:

$$DL = \frac{1}{N} \sum_{j=1}^N \sum_{k \in N(j)} t_{kj} \vec{e}_{kj} \otimes \vec{e}_{kj},$$

7

The PZ tensor is a third-order symmetric tensor. According to the above discussion, the edge-based expansion formula of the PZ tensor is given as follows:

$$PZ = \frac{1}{N} \sum_{j=1}^N \left(\sum_{k \in N(j)} t_{kj} (\vec{e}_{kj})^{\otimes 3} + \sum_{\substack{k, i \in N(j) \\ k \neq i}} t_{kji} \vec{e}_{kj} \otimes (\vec{e}_{ji})^{\otimes 2} \right)$$

8

The first term is constructed by the 3-fold tensor product of \vec{e}_{kj} , and the second term is constructed by the tensor product of \vec{e}_{kj} with the 2-fold tensor product of \vec{e}_{ji} . Both terms satisfy the symmetry of $T_{abc} = T_{acb}$.

Network implementation

In traditional GNNs, the features of each atom are embedded in a high-dimensional space and updated by passing messages between atoms. The contribution of each atom to the scalar property of a crystal is finally obtained through an atom-wise regression neural network. According to the tensor prediction framework discussed in the previous section, the expansion coefficients of tensors up to order three are mapped from the features of the edges or the triplets. In this work, we designed the edge-based tensor prediction graph neural network (ETGNN), which is a modified version of DimeNet++³⁸. Although in principle any common GNN can be adopted to predict tensor properties within our framework, here we adopt DimeNet++ as it is an invariant GNN that was shown to have high precision in the prediction of scalar properties^{22, 38}. ETGNN obtains the tensor expansion coefficients by updating the learned embeddings of the edges and the triplets in the crystal graphs.

ETGNN has inherited the directional message passing framework used by DimeNet++, i.e. the atom features h_j, h_i and the edge features $u_{ij}^{(k)}$ of atom pairs ji are integrated into the directional edge message $m_{ji}^{(k)}$ being sent from atom j to atom i , where k is the index of the multiplicity of the edges.

Furthermore, ETGNN introduces an additional triplet component in the crystal graph, which is composed of node j and its two neighbor nodes k and i . The nodes, edges, and angles contained in the triplets are embedded into the triplet messages m_{kji} . Using equivariant expressions of tensors proposed in the present work, ETGNN can predict both scalars and various tensor properties, such as forces \vec{F} , BECs, DL, and PZ tensors. ETGNN can realize the following mapping:

$$f_{\theta} : \left\{ m_{kj}^{(k_1)}, \dots, m_{ji}^{(k_2)}, \dots, m_{kji}^{(k_1, k_2)}, \dots \right\} \rightarrow R, \vec{F}, BEC, DL, PZ, \dots$$

9

where θ is the learnable parameters of the network.

The architecture of ETGNN is shown in Fig. 2a. We kept the existing architecture in DimeNet++ and introduced the triplet embedding and the triplet update blocks. For tensor prediction, an edge-wise layer φ_{edge} and a triplet-wise layer $\varphi_{triplet}$ are used to get the coefficients in the tensor expansion:

$$t_{kj} = \varphi_{edge}(m_{kj}), t_{kji} = \varphi_{triplet}(m_{kji}).$$

Triplet embedding block. The triplet embedding block is shown in Fig. 2b. The triplet message is embedded based on the distances $|\vec{r}_{kj}|$ and $|\vec{r}_{ji}|$ between node j and its neighbor nodes k and i , the angle α_{kji} between \vec{r}_{kj} and \vec{r}_{ji} , and the atomic numbers Z_k, Z_j and Z_i . The spherical Bessel function $\varphi_{SBF} : (R^1, R^1) \rightarrow R^{N_{SRBF} \cdot N_{SHBF}}$ is used as the two-dimensional joint bases of the distances $|\vec{r}_{kj}|$ and the angles α_{kji} in the triplets:

$$\phi_{SBF}(|\vec{r}_{kj}|, \alpha_{kji}) = \sqrt{\frac{2}{r_c^3 J_{l+1}^2(z_{ln})}} j_l\left(\frac{z_{ln}}{r_c} |\vec{r}_{kj}|\right) Y_l^0(\alpha_{kji})$$

,

10

where j_l is the first kind spherical Bessel function of order l , and z_{ln} is its n th root, $0 \leq l \leq N_{SHBF} - 1$, $1 \leq n \leq N_{SRBF}$. The expansion coefficients of the spherical Bessel function are multiplied by the cosine cutoff function to obtain the two-dimensional joint basis representation of $|\vec{r}_{kj}|$ and α_{kji} :

$a_{SBF}^{(kj,ji)} = f_c\left(|\vec{r}_{kj}|\right) \varphi_{SBF}\left(|\vec{r}_{kj}|, \alpha_{kji}\right)$. Then the coefficients of the basis functions are linearly combined through a self-interaction layer $\phi_{SBF} : R^{N_{SRBF} \cdot N_{SHBF}} \rightarrow R^{n_{tri}}$, where n_{tri} is the number of the hidden features of the triplets and $n_{tri} = 128$ in this work. According to $a_{SBF}^{(kj,ji)}$, $e_{RBF}^{(ji)}$ and atomic numbers Z_k, Z_j and Z_i , the embedding of the triplet can be constructed in the following formula:

$$m_{kji}^{(0)} = \sigma \left[W \left(g(Z_i) \oplus g(Z_j) \oplus g(Z_k) \oplus \varphi_{SBF} \left(a_{SBF}^{(kj,ji)} \right) \oplus \varphi_{RBF} \left(e_{RBF}^{(ji)} \right) \right) + b \right],$$

where σ is ELU activation function³⁹, g is a learnable atomic embedding layer.

Triplet update block. The embeddings of edge messages and triplet messages are updated through multiple edge update blocks and triplet update blocks. The goal of ETGNN is just to achieve the prediction of the tensor properties, so the edge update block adopts the original interaction layer in DimeNet++ to ensure that the modified network has the same accuracy as the original one. The triplet update block uses the directional message passing mechanism similar to that in the edge update block. The update of the features of the triplets can be expressed by the following formula:

$$m_{kji}^{(t+1)} = f_{update} \left(m_{kji}^{(t)}, f_{int} \left(m_{kj}^{(t)}, m_{ji}^{(t)}, e_{RBF}^{(kj)}, e_{RBF}^{(ji)}, a_{SBF}^{(kj,ji)} \right) \right),$$

12

where f_{update} and f_{int} are update function and interaction function respectively, which are implemented by neural networks. The hidden features of the triplets $m_{kji}^{(t)}$ are updated using the directional edge messages $m_{kj}^{(t)}$ and $m_{ji}^{(t)}$ at the same layer. The angle α_{kji} between the directional edge messages $m_{kj}^{(t)}$ and $m_{ji}^{(t)}$ is also explicitly embedded in the spherical Bessel function $a_{SBF}^{(kj,ji)}$ to update $m_{kji}^{(t)}$.

Tests and applications

We trained ETGNN with the forces of the molecular dynamics (MD) trajectories of the extended systems provided in ref.⁴⁰. The extended systems consist of the supercells of inorganic and organic crystals and also contain clusters, high entropy alloys (HEA), and two-dimensional materials. The organic polymer pyridine and bulk TiO_2 contain two and three phases respectively, which can test the prediction accuracy of the model for different phases. High entropy alloy (HEA) CoCrFeMnNi contains five metal elements and each element is randomly arranged in the crystal, which is a great challenge to the model. DeepPot-SE⁴⁰ and DeePMD⁴¹ are two representative neural network potential energy surface (PES) models, which calculate the forces by using the gradients of the potential energy: $\vec{F}_i = -\nabla_i E$. For each sub-systems, 90% randomly selected structures are used for training, and the remaining 10% are used for testing⁴⁰. As can be seen from Table 1, the ETGNN model achieved lower RMSEs than DeepPot-SE and DeePMD on nearly all the sub-systems.

Table 1

Comparison of the root mean square errors (RMSEs) of the predicted forces for the extended systems by ETGNN, DeepPot-Se, and DeepPMD. The lowest RMSE among the considered models for each subsystem is displayed in bold. The unit is meV/Å.

System	Sub-system	DeepPot-Se	DeepPMD	ETGNN
Bulk Cu	FCC solid	90	90	89
Bulk Ge	Diamond solid	38	35	7
Bulk Si	Diamond solid	36	31	5
Bulk Al ₂ O ₃	Trigonal solid	49	55	36
Bulk C ₅ H ₅ N	Pyridine-I	25	25	14
	Pyridine-II	39	39	19
Bulk TiO ₂	Rutile	137	163	61
	Anatase	181	216	82
	Brookite	94	109	44
MoS ₂ + Pt	MoS ₂ slab	23	34	27
	bulk Pt	84	226	27
	Pt surface	105	187	37
	Pt cluster	201	255	68
	Pt on MoS ₂	94	127	33
CoCrFeMnNi HEA	rand. occ. I	394	481	373
	rand. occ. II	410	576	385

Similar to the atomic force, some other tensors can be obtained as the first or second partial derivative of the energy with respect to the external field⁴². Here we compare the previous gradient-based tensor prediction method with our ETGNN models. We have successfully trained the ETGNN models on the dataset of the first-order dipole moment μ , the second-order polarizability tensor α , and the atomic second-order chemical shift tensors σ of two organic molecules of ethanol and allyl p-tolyl ether. The expansion formulas of the dielectric tensor and Born effective charge tensor were used to decompose the polarizability and the atomic chemical shift tensor respectively. We compared the results of ETGNN with FieldSchNet⁴² which computes these response properties using derivatives of total energies. Table 2 shows the comparison of the mean absolute errors (MAEs) of ETGNN and FieldSchNet trained on ethanol in vacuum and allyl p-tolyl ether in vacuum. As can be seen from Table 2, the prediction error of ETGNN for almost all the tensor properties listed in Table 2 is much smaller than that of FieldSchNet.

Table 2

Comparison of the mean absolute errors (MAEs) of ETGNN and FieldSchNet trained on ethanol in vacuum and allyl p-tolyl ether in vacuum. The lowest MAE between the two models for each property is displayed in bold.

Property	Unit	allyl p-tolyl ether (vacuum)		ethanol (vacuum)	
		FieldSchNet	ETGNN	FieldSchNet	ETGNN
μ	D	0.003	0.00024	0.004	0.0018
α	Bohr ³	0.039	0.0202	0.008	0.025
σ_{all}	ppm	0.273	0.0293	0.169	0.00735
σ_{C}	ppm	0.301	0.0417	0.194	0.00721
σ_{H}	ppm	0.045	0.0202	0.123	0.00385
σ_{O}	ppm	2.732	0.0147	0.401	0.00286

Based on the tensor expansion formulas, we tested the prediction accuracy of ETGNN for the BECs, the DL tensors ϵ_{∞} (electronic contribution), and the PZ tensors of crystals. The training datasets are from the density functional perturbation theory (DFPT) calculations on 3190 Al₂O₃, 3992 SiO₂, 10000 HfO₂, 3211 AlN, 3000 CdS, and 3000 ZnO random perturbed structures. HfO₂ is a potential complementary metal-oxide-semiconductor (CMOS) compatible ferroelectric memory material and can form many crystal structures⁴³⁻⁴⁶. The perturbed structures of HfO₂ consist of 5000 structures with 6-coordinated Hf ions and 5000 structures with 8-coordinated Hf ions. Each model was trained with 60% of the data, validated with 20% of the data, and tested with the remaining 20% of the data. The comparisons of the DFT calculated tensors and the ETGNN predicted tensors on the test datasets of the perturbed structures are shown in Fig. 3. As shown in Fig. 3(a - c), each component of the BECs predicted by ETGNN is very close to the corresponding component of the BECs calculated by DFT. The mean absolute errors (MAEs) of the components of the predicted BECs on Al₂O₃, SiO₂, and HfO₂ test sets are only $1.18 \times 10^{-2} e$, $4.28 \times 10^{-3} e$, and $1.94 \times 10^{-3} e$, respectively. The MAEs of the components of the predicted ϵ_{∞} on Al₂O₃, SiO₂, and HfO₂ test sets are only 5.54×10^{-3} , 1.98×10^{-3} and 2.86×10^{-3} , respectively. For the third-order PZ tensor, ETGNN still maintains a high prediction accuracy. The MAEs of the components of the predicted PZ tensors on AlN, CdS, and ZnO test sets are only $3.29 \times 10^{-4} \text{ C/m}^2$, $4.69 \times 10^{-4} \text{ C/m}^2$, and $5.59 \times 10^{-4} \text{ C/m}^2$, respectively. The tensor prediction test on these perturbed structures indicates that invariant GNNs can achieve high prediction accuracy in principle by using the edge-based tensor expressions proposed in this work.

ETGNN has also been tested on the BECs and DL tensors ϵ_{∞} of about 5000 non-metallic materials in the JARVIS-DFT database⁴⁷. The comparison of the predicted values and the target values on the JARVIS-

DFT dataset can be seen in Fig. S2 (Supplementary). This dataset contains more than 80 elements in the periodic table. The structures containing some rare earth elements in this dataset may have large calculation errors because the pseudopotentials are often hard to accurately describe the complex electronic structures of the rare earth elements. This will affect the prediction performance of the ML methods. For the JARVIS-DFT data set, 70%, 20%, and 10% of the calculated values were used as the training, validation, and test set, respectively. The MAE of ETGNN on the test set of BECs still reached a low value of 0.045 e. This high prediction accuracy means that ETGNN can be used as a universal model for calculating BECs with a much faster speed than DFT.

For comparison with the traditional ML models, an ETGNN model was trained for maximum BECs in the JARVIS-DFT dataset. For the maximum component of the BECs, the MAE of the ETGNN model on the test set is 0.12 e, which is only one fifth of that of the classical force-field inspired descriptors (CFID) model used in ref. ⁴⁷. It was reported that large deviations between the experimental and the calculated dielectric constants can be seen for approximately 20% of the compounds⁴⁸. Thus predicting the dielectric tensors of various crystals was thought to be a huge challenge. The ETGNN regression model for the dielectric tensors was successfully trained and achieved an MAE of 0.21 on the test dataset.

ETGNN automatically develops physical insights into the Born effective charge of materials while training on the JARVIS-DFT dataset. It can be observed from Fig. 4 that the embedded features from the ETGNN model trained for the mean diagonal value of BECs have a distinct separation for atoms with different mean diagonal values. The mean diagonal values of the data points in the principal component analysis (PCA) projection plot gradually increase from the upper left side to the upper right side. The mean diagonal values of the BECs of metal elements in oxides are positive, while the mean diagonal values of some group VIII metal elements such as Ru, Fe, and Co in multi-element alloys have negative minima. The mean diagonal values of group VA, VIA, and VIIA non-metallic elements increase sequentially. The BECs of atoms in some single-element crystals, such as Si and He, are almost zero, lying on the borderline between positive and negative BECs in the PCA projection plot. The mean diagonal values of hydrogen, alkali, group IIA, and group IIIA metal elements are positive and increase sequentially. Some transition metal cations have larger mean diagonal values of BECs than other elements and are located in the region closer to the upper right corner. The representation learned by ETGNN can be used to characterize and understand the large chemical space of the BECs of the materials.

In conclusion, we generalized the atom-centric framework of GNNs to tensors and proposed a general tensor prediction framework that decomposes the tensorial properties by the local spatial components projected on the edge directions of multiple-sized clusters. Based on this idea, we have given the explicit formula of the body-ordered expansions of general tensors. These expansions are rotationally equivalent, while the coefficients in the expansions are invariant and can be predicted by various traditional invariant GNNs. We designed ETGNN based on an invariant GNN to verify our tensor prediction framework. The precision of ETGNN outperforms the state-of-the-art models on a variety of tensor prediction tasks. For the force prediction on the extended systems, ETGNN outperforms DeePMD and DeepPot-SE on nearly all of the test systems. This shows that ETGNN can be used for precise potential fields of various molecules

and crystals. For the response properties including the first-order dipole moment μ , the second-order polarizability tensor α , and the atomic second-order chemical shift tensors σ , ETGNN achieved much higher accuracy than that of FieldSchNet. This shows that ETGNN has a strong fitting ability for the response properties of various external fields. ETGNN was also used to predict the BECs, DL, and PZ tensors of the random perturbed structures and achieved very high accuracy. The evaluation of ETGNN on these perturbed structures indicates that the tensor expansions proposed in this work are valid and general. Besides, we have successfully trained the regression models of ETGNN for predicting the BECs and DL tensors of about 5000 non-metallic materials containing more than 80 elements. Previous work could not handle the tensors and only successfully trained the regression models for the maximum component of these tensors⁴⁷. Taking into account the errors of the tensors calculated by DFPT, the mean absolute error of the predicted tensors in this dataset is relatively low. Our study suggests that ETGNN is a general, efficient and accurate framework for GNNs to predict the tensorial properties.

Method

Pytorch⁴⁹, PyG⁵⁰, and Pytorch Lightning libraries are used to implement ETGNN. The Pymatgen⁵¹ library is used to read the crystal structures and search the neighbor atoms around each atom. We expand the distance of each edge with 6 radial Bessel functions and transform the expansion coefficients into the 128-dimensional edge message features through a self-interaction layer. Spherical Bessel functions are used as a joint representation of the distances and angles for the triplets and are embedded into the 128-dimensional triplet message features. The edge message features are refined through the original interaction layer in DimeNet++³⁸, while the triplet features are refined through the triplet update block proposed in this work. ETGNN has used 4 edge and triplet update blocks in all experiments in this work. Each tensor expansion coefficient is mapped from the refined edge message features or refined triplet message features by a 3-layer MLP respectively. The hyperparameters for all the reported experiments and details on the search for the optimal hyperparameters are provided in Supplementary Table S2 and Supplementary Discussion 2, respectively. We flatten the algebraic difference of the predicted tensor and the target tensor into a 1D vector, whose Euclidean norm (i.e, L2 norm) is used as the loss function. The proof of the invariance of the Euclidean loss function of the tensors can be found in Supplementary Discussion 3.

The Born effective charges, dielectric and piezoelectric tensors in the training sets were calculated by the density functional perturbation theory (DFPT) implemented in the Vienna Ab-initio simulation package (VASP)⁵². The exchange and correlation interaction of electrons was treated with the generalized gradient approximation (GGA) of Perdew-Burke-Ernzerhof (PBE) functional⁵³.

Declarations

DATA AND CODE AVAILABILITY

The data and code that support the results of this work are available from the corresponding author upon reasonable request.

ACKNOWLEDGEMENTS

This work is supported by NSFC (Grants No. 811825403, No. 11991061, and No. 12188101) and Guangdong Major Project of Basic and Applied Basic Research (Future functional materials under extreme conditions - 2021B0301030005).

AUTHOR CONTRIBUTIONS

H.J.X., Y.Z., and H.Y.Y. proposed the research and the methodology in this work. Y.Z. coded ETGNN and wrote the manuscript. H.Y.Y, H.J.X, and X.G.G. revised the manuscript. All authors discussed the results.

COMPETING INTERESTS

The authors declare no competing interests.

References

1. Butler, K. T., Davies, D. W., Cartwright, H., Isayev, O. & Walsh, A. Machine learning for molecular and materials science. *Nature* **559**, 547–555 (2018).
2. Pollice, R. et al. Data-Driven Strategies for Accelerated Materials Design. *Acc. Chem. Res.* **54**, 849–860 (2021).
3. Morgan, D. & Jacobs, R. Opportunities and Challenges for Machine Learning in Materials Science. *Annu. Rev. Mater. Res.* **50**, 71–103 (2020).
4. Hart, G. L. W., Mueller, T., Toher, C. & Curtarolo, S. Machine learning for alloys. *Nat. Rev. Mater.* **6**, 730–755 (2021).
5. Lu, S. H. et al. Accelerated discovery of stable lead-free hybrid organic-inorganic perovskites via machine learning. *Nat. Commun.* **9**, 3405 (2018).
6. Cai, X. et al. Discovery of Lead-Free Perovskites for High-Performance Solar Cells via Machine Learning: Ultrabroadband Absorption, Low Radiative Combination, and Enhanced Thermal Conductivities. *Adv. Sci.* e2103648 (2021).
7. Kitchin, J. R. Machine learning in catalysis. *Nat. Catal.* **1**, 230–232 (2018).
8. Ma, S. C. & Liu, Z. P. Machine Learning for Atomic Simulation and Activity Prediction in Heterogeneous Catalysis: Current Status and Future. *Acs. Catal.* **10**, 13213–13226 (2020).
9. Zhang, N. et al. Machine Learning in Screening High Performance Electrocatalysts for CO₂ Reduction. *Small Methods* **5**, 2100987 (2021).
10. Liu, Y. T., Zhou, Q. & Cui, G. L. Machine Learning Boosting the Development of Advanced Lithium Batteries. *Small Methods* **5**, 2100442 (2021).

11. Lv, C. D. et al. Machine Learning: An Advanced Platform for Materials Development and State Prediction in Lithium-Ion Batteries. *Adv. Mater.* 2101474 (2021).
12. Wang, T., Zhang, C., Snoussi, H. & Zhang, G. Machine Learning Approaches for Thermoelectric Materials Research. *Adv. Funct. Mater.* **30**, 1906041 (2019).
13. Chmiela, S. et al. Machine learning of accurate energy-conserving molecular force fields. *Sci. Adv.* **3**, e1603015 (2017).
14. Fonseca, G., Poltavsky, I., Vassilev-Galindo, V. & Tkatchenko, A. Improving molecular force fields across configurational space by combining supervised and unsupervised machine learning. *J. Chem. Phys.* **154**, 124102 (2021).
15. Vassilev-Galindo, V., Fonseca, G., Poltavsky, I. & Tkatchenko, A. Challenges for machine learning force fields in reproducing potential energy surfaces of flexible molecules. *J. Chem. Phys.* **154**, 094119 (2021).
16. Cheng, Z. et al. Building quantum mechanics quality force fields of proteins with the generalized energy-based fragmentation approach and machine learning. *Phys. Chem. Chem. Phys.* **24**, 1326–1337 (2022).
17. Schutt, K. T., Arbabzadah, F., Chmiela, S., Muller, K. R. & Tkatchenko, A. Quantum-chemical insights from deep tensor neural networks. *Nat. Commun.* **8**, 13890 (2017).
18. Schutt, K. T., Sauceda, H. E., Kindermans, P. J., Tkatchenko, A. & Muller, K. R. SchNet - A deep learning architecture for molecules and materials. *J. Chem. Phys.* **148**, 241722 (2018).
19. Xie, T. & Grossman, J. C. Crystal Graph Convolutional Neural Networks for an Accurate and Interpretable Prediction of Material Properties. *Phys. Rev. Lett.* **120**, 145301 (2018).
20. Unke, O. T. & Meuwly, M. PhysNet: A Neural Network for Predicting Energies, Forces, Dipole Moments, and Partial Charges. *J. Chem. Theory Comput.* **15**, 3678–3693 (2019).
21. Park, C. W. & Wolverton, C. Developing an improved crystal graph convolutional neural network framework for accelerated materials discovery. *Phys. Rev. Mater.* **4**, 063801 (2020).
22. Klicpera, J., Gro, J. & Günnemann, S. Directional Message Passing for Molecular Graphs. Preprint at <https://arxiv.org/abs/2003.03123v1> (2020).
23. Haghighatlari, M. et al. Learning to Make Chemical Predictions: the Interplay of Feature Representation, Data, and Machine Learning Algorithms. *Chem.* **6**, 1527–1542 (2020).
24. Unke, O. T. & Meuwly, M. A reactive, scalable, and transferable model for molecular energies from a neural network approach based on local information. *J. Chem. Phys.* **148**, 241708 (2018).
25. Faber, F. A., Christensen, A. S., Huang, B. & von Lilienfeld, O. A. Alchemical and structural distribution based representation for universal quantum machine learning. *J. Chem. Phys.* **148**, 241717 (2018).
26. Bartok, A. P., Kondor, R. & Csanyi, G. On representing chemical environments. *Phys. Rev. B* **87**, 184115 (2013).
27. Thomas, N. et al. Tensor field networks: Rotation- and translation-equivariant neural networks for 3D point clouds. Preprint at <https://arxiv.org/abs/1802.08219v3> (2018).

28. Weiler, M., Geiger, M., Welling, M., Boomsma, W. & Cohen, T. 3D Steerable CNNs: Learning Rotationally Equivariant Features in Volumetric Data. Preprint at <https://arxiv.org/abs/1807.02547v2> (2018).
29. Batzner, S. et al. E(3)-Equivariant Graph Neural Networks for Data-Efficient and Accurate Interatomic Potentials. Preprint at <https://arxiv.org/abs/2101.03164v3> (2021).
30. Brandstetter, J., Hesselink, R., Elise, V., Bekkers, E. & Welling, M. Geometric and Physical Quantities improve E(3) Equivariant Message Passing. Preprint at <https://arxiv.org/abs/2110.02905v2> (2021).
31. Batzner, S. et al. E(3)-equivariant graph neural networks for data-efficient and accurate interatomic potentials. *Nat. Commun.* **13**, (2022).
32. Batatia, I. et al. The Design Space of E(3)-Equivariant Atom-Centered Interatomic Potentials. Preprint at <https://arxiv.org/abs/2205.06643v1> (2022).
33. Musaelian, A. et al. Learning Local Equivariant Representations for Large-Scale Atomistic Dynamics. Preprint at <https://arxiv.org/abs/2204.05249v1> (2022).
34. Grisafi, A., Wilkins, D. M., Csanyi, G. & Ceriotti, M. Symmetry-Adapted Machine Learning for Tensorial Properties of Atomistic Systems. *Phys. Rev. Lett.* **120**, 036002 (2018).
35. Nguyen, V. H. A. & Lunghi, A. Predicting tensorial molecular properties with equivariant machine-learning models. Preprint at <https://arxiv.org/abs/2202.01449v1> (2022).
36. Glick, Z. L., Koutsoukas, A., Cheney, D. L. & Sherrill, C. D. Cartesian message passing neural networks for directional properties: Fast and transferable atomic multipoles. *J. Chem. Phys.* **154**, 224103 (2021).
37. Behler, J. & Parrinello, M. Generalized neural-network representation of high-dimensional potential-energy surfaces. *Phys. Rev. Lett.* **98**, 146401 (2007).
38. Klicpera, J., Giri, S., Margraf, J. T. & Günnemann, S. Fast and Uncertainty-Aware Directional Message Passing for Non-Equilibrium Molecules. Preprint at <https://arxiv.org/abs/2011.14115> (2020).
39. Clevert, D.-A., Unterthiner, T. & Hochreiter, S. Fast and Accurate Deep Network Learning by Exponential Linear Units (ELUs). Preprint at <https://doi.org/10.48550/arXiv.1511.07289> (2015).
40. Zhang, L. F. et al. End-to-end Symmetry Preserving Inter-atomic Potential Energy Model for Finite and Extended Systems. *Adv. Neur. In.* **31**, 4441–4451 (2018).
41. Wang, H., Zhang, L. F., Han, J. Q. & E, W. N. DeePMD-kit: A deep learning package for many-body potential energy representation and molecular dynamics. *Comput. Phys. Commun.* **228**, 178–184 (2018).
42. Gastegger, M., Schutt, K. T. & Müller, K. R. Machine learning of solvent effects on molecular spectra and reactions. *Chemical Science* **12**, 11473–11483 (2021).
43. Park, M. H., Lee, Y. H., Mikolajick, T., Schroeder, U. & Hwang, C. S. Review and perspective on ferroelectric HfO₂-based thin films for memory applications. *Mrs Commun.* **8**, 795–808 (2018).
44. Gutowski, M. et al. Thermodynamic stability of high-K dielectric metal oxides ZrO₂ and HfO₂ in contact with Si and SiO₂. *Appl. Phys. Lett.* **80**, 1897–1899 (2002).

45. Boescke, T. S., Muller, J., Brauhaus, D., Schroder, U. & Bottger, U. Ferroelectricity in hafnium oxide thin films. *Appl. Phys. Lett.* **99**, 102903 (2011).
46. Pesic, M. et al. A computational study of hafnia-based ferroelectric memories: from ab initio via physical modeling to circuit models of ferroelectric device. *J. Comput. Electron.* **16**, 1236–1256 (2017).
47. Choudhary, K. et al. High-throughput density functional perturbation theory and machine learning predictions of infrared, piezoelectric, and dielectric responses. *Npj Comput. Mater.* **6**, 64 (2020).
48. Umeda, Y., Hayashi, H., Moriwake, H. & Tanaka, I. Prediction of dielectric constants using a combination of first principles calculations and machine learning. *Jpn. J. Appl. Phys.* **58**, SLLC01–SLLC01 (2019).
49. Paszke, A., Gross, S., Massa, F., Lerer, A. & Chintala, S. PyTorch: An Imperative Style, High-Performance Deep Learning Library. Preprint at <https://arxiv.org/abs/1912.01703> (2019).
50. Fey, M. & Lenssen, J. E. Fast Graph Representation Learning with PyTorch Geometric. Preprint at <https://arxiv.org/abs/1903.02428v3> (2019).
51. Ong, S. P. et al. Python Materials Genomics (pymatgen): A robust, open-source python library for materials analysis. *Comp. Mater. Sci.* **68**, 314–319 (2013).
52. Kresse, G. & Furthmuller, J. Efficiency of ab-initio total energy calculations for metals and semiconductors using a plane-wave basis set. *Comp. Mater. Sci.* **6**, 15–50 (1996).
53. Perdew, J. P., Burke, K. & Ernzerhof, M. Generalized gradient approximation made simple. *Phys. Rev. Lett.* **77**, 3865–3868 (1996).

Figures

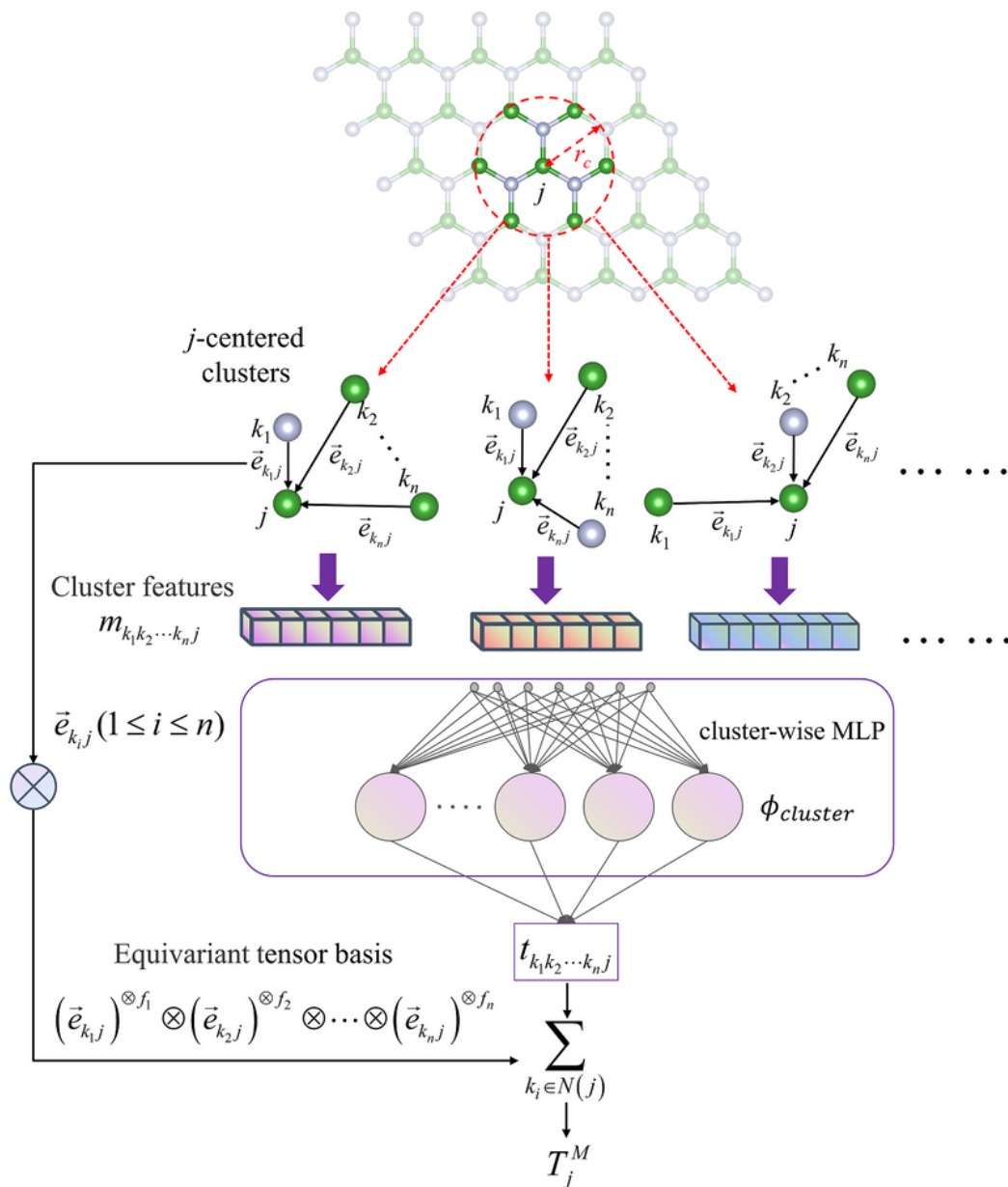


Fig. 1 The schematic diagram of predicting the atomic rank- M tensors. The atomic rank- M tensors are expanded with the rank- M tensor bases constructed by M edge vectors which contain n ($n \leq M$) individual neighbor atoms within a cutoff radius r_c . For symmetric tensor bases, the required number of individual neighbor atoms n can be less than M by using multi-fold tensor products of the edge vectors. The n individual neighbor atoms together with the central atom j form a cluster containing $(n+1)$ atoms. The lengths of the edges and the angles between the edges in the cluster can be aggregated into a feature vector $m_{k_1k_2 \dots k_nj}$ that can be updated iteratively. The corresponding tensor expansion coefficients $t_{k_1k_2 \dots k_nj}$ are mapped from the features of each cluster through a cluster-wise regression layer $\phi_{cluster}$. The tensor of atom j is obtained by summing the tensor contributions of each j -centered cluster.

Figure 1

See image above for figure legend.

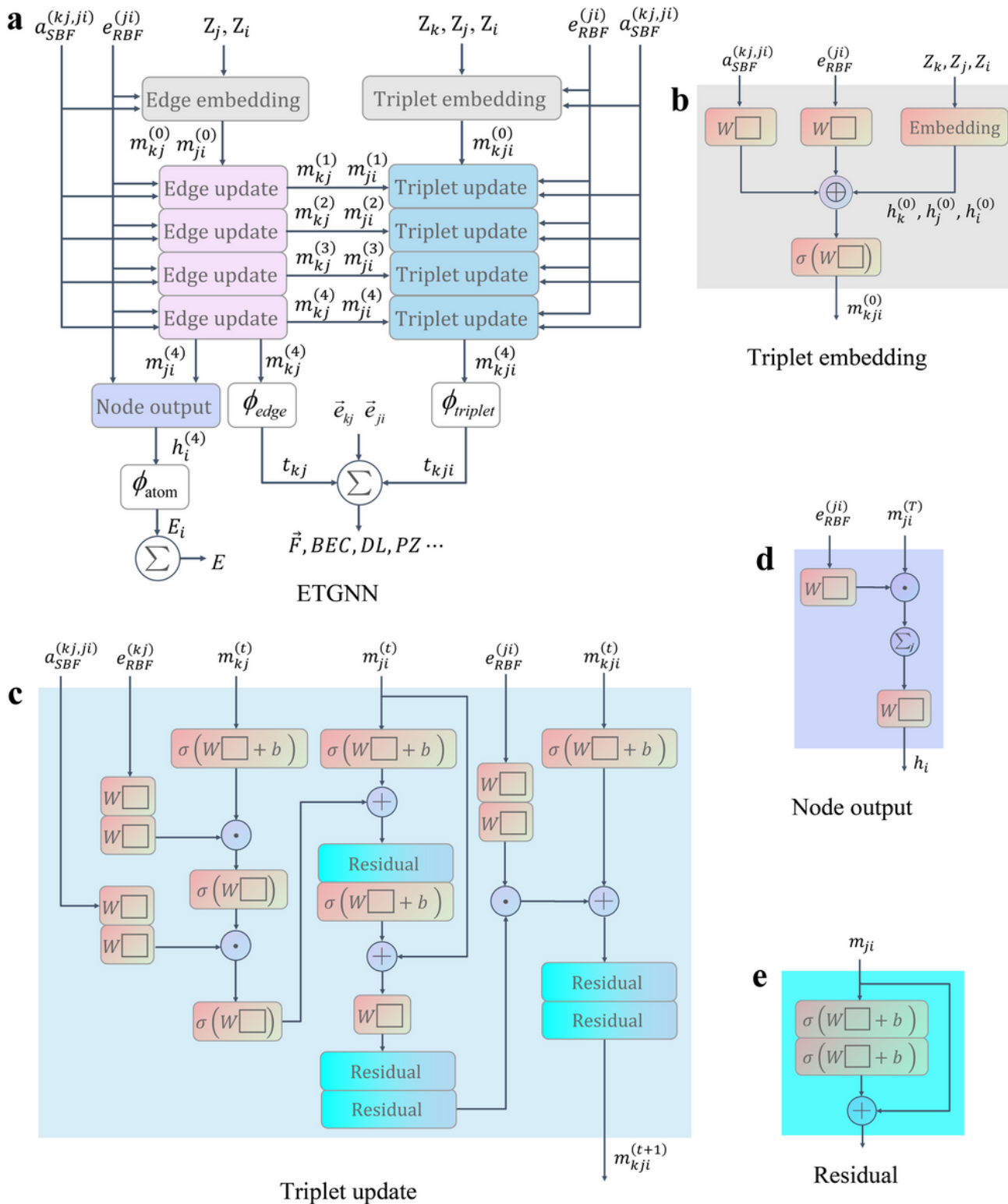


Figure 2

The architecture of ETGNN and its sub-networks. **a** is the architecture of ETGNN with four layers of edge and triplet update blocks. The edge embedding and edge update blocks are inherited from the original embedding and interaction blocks of DimeNet++ respectively so that the high precision of DimeNet++ can be retained. The initial features of the triplets are generated in **b** the triplet embedding block and are updated through **c** the triplet update blocks. The output of the last edge update block can be aggregated

into the node features for scalar outputs by the **d** node output block. **e** shows the residual block²⁰, which is a multilayer feedforward neural network with a shortcut connection to avoid the vanishing gradients problem.

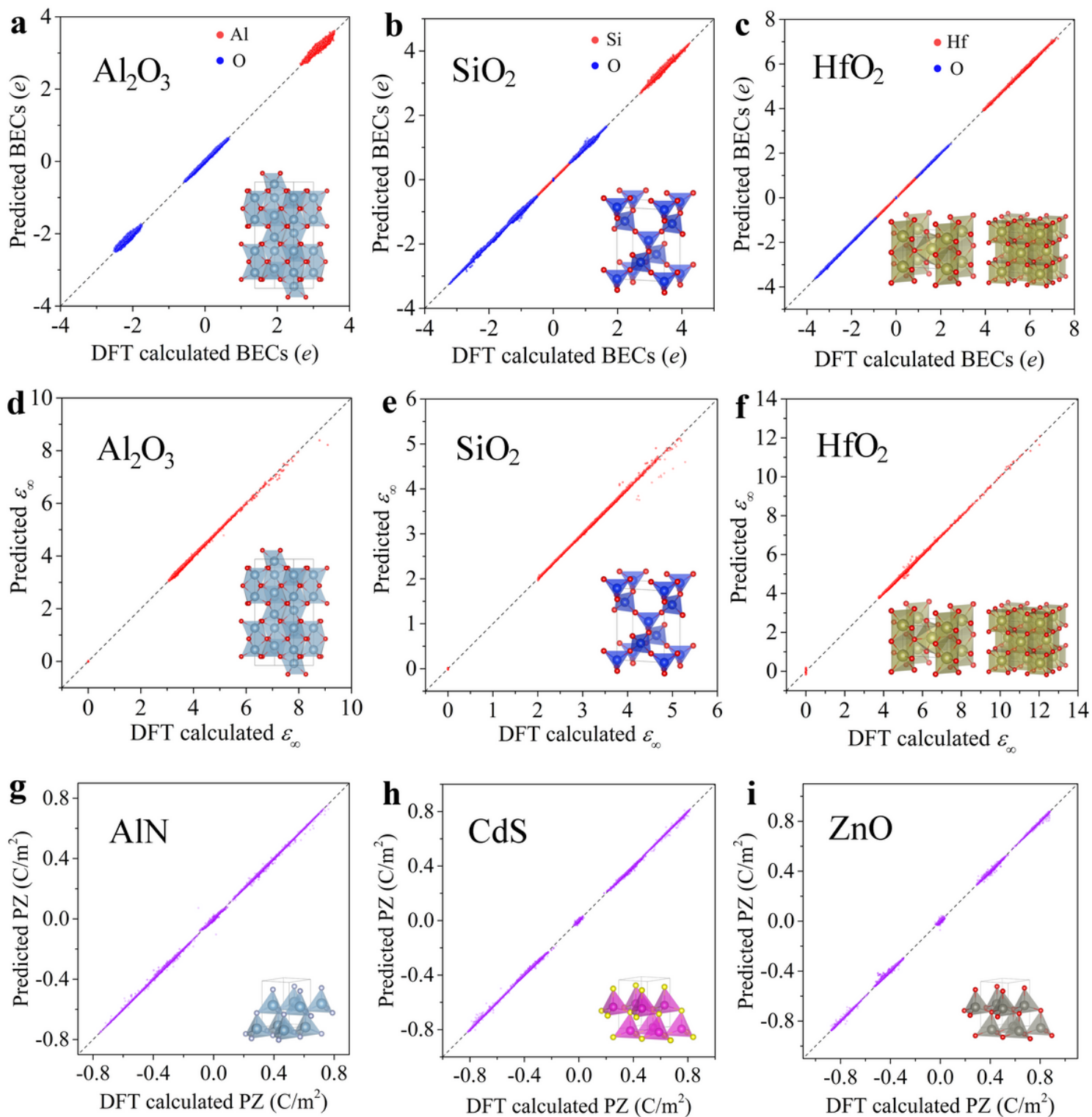


Figure 3

Comparison of ETGNN predicted values and the DFT calculated values on the BECs (**a-c**), DL (**d-f**), and PZ (**g-i**) tensors of the testing perturbed structure dataset.

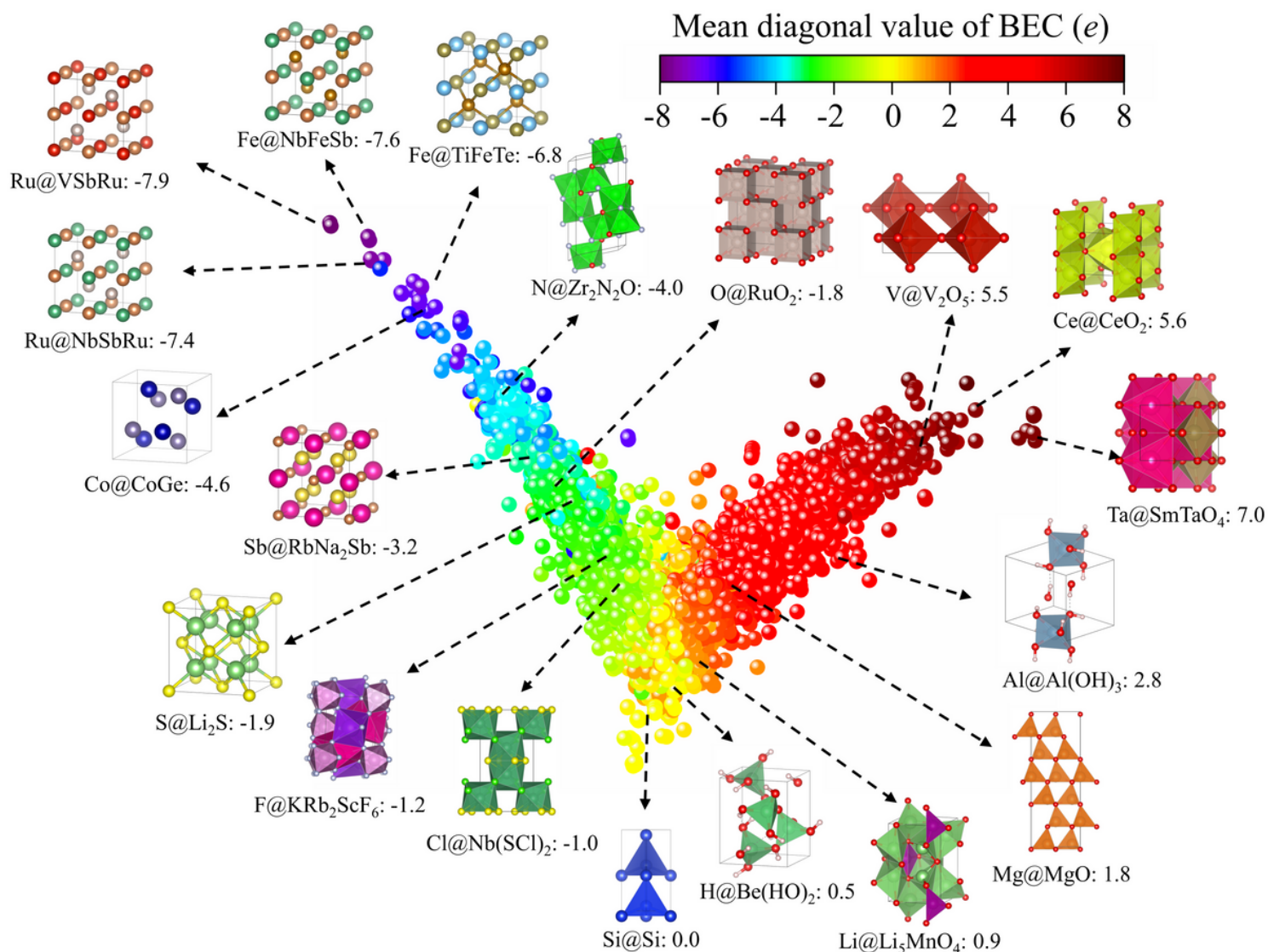


Figure 4

Visualizing the embedding space of the atoms in the JARVIS-DFT dataset using PCA. Each point on the graph is colored according to the mean diagonal value of the BEC of each atom.

Supplementary Files

This is a list of supplementary files associated with this preprint. Click to download.

- [SupplementaryMaterials.pdf](#)